AGU100 ADVANCING EARTH AND SPACE SCIENCE

JGR

Journal of Geophysical Research: Planets

RESEARCH ARTICLE
10.1029/2018JE005647

Special Section:
Science and Exploration of the Moon, Near-Earth Asteroids, and the Moons of Mars

MGS-TES Spectra Suggest a Basaltic Component in the Regolith of Phobos

Timothy D. Glotch[1], Christopher S. Edwards[2], Mehmet Yesiltas[3], Katherine A. Shirley[1], Dylan S. McDougall[1], Alexander M. Kling[1], Joshua L. Bandfield[4], and Christopher D. K. Herd[5]

[1]Department of Geological Sciences, Stony Brook University, Stony Brook, NY, USA, [2]Northern Arizona University, Flagstaff, AZ, USA, [3]Kirklareli University, Kirklareli, Turkey, [4]Space Science Institute, Boise, ID, USA, [5]University of Alberta, Edmonton, Alberta, Canada

Abstract The origins of the Martian moons Phobos and Deimos have been the subjects of considerable debate. Visible and near-infrared spectra of these bodies are dark and nearly featureless, with red slopes of varying degrees. These spectra are generally consistent with those of carbonaceous asteroids, leading to the hypothesis that Phobos and Deimos are captured carbonaceous asteroids. The shapes and inclinations of the orbits of Phobos and Deimos present problems for the asteroid capture hypothesis. This had led researchers to suggest that Phobos and Deimos coaccreted with Mars or that they are the result of an impact with Mars or in the Mars vicinity. In this work, we reexamine Mars Global Surveyor Thermal Emission Spectrometer (MGS-TES) data of Phobos and compare spectra of the Phobos surface to mid-IR spectra of the ungrouped C2 meteorite Tagish Lake (a suggested analog for D-class asteroids) and particulate basalt and phyllosilicate samples (mixed with carbon black to reduce their visible albedos) acquired in a simulated airless body environment. We find that Tagish Lake is a poor mid-IR spectral analog to Phobos and that major spectral features in the Phobos spectrum are best matched by a silicate transparency feature similar to that found for finely particulate basalt. Other features in the spectrum are likely best explained by a phyllosilicate component. We suggest that these results indicate that at a portion of the Phobos surface regolith is derived from the Martian crust.

Plain Language Summary The Martian moons Phobos and Deimos have been suggested to be captured asteroids based on the similarities between the dark, red, nearly featureless visible and near-infrared spectra of these bodies and carbonaceous asteroids. However, the capture hypothesis suffers from difficulties associated with the shapes and inclinations of the moons' orbits. Alternatively, Phobos and Deimos have been suggested to originate from an impact with, or in the vicinity of, Mars. In this work, we examine midinfrared spectra of Phobos and compare them with spectra of different materials acquired in the laboratory under simulated airless body conditions. We find that the mid-IR spectra of Phobos are most consistent with the presence of a basaltic component, perhaps with admixed phyllosilicates. As the Martian crust is mostly composed of basaltic rocks, we suggest that Phobos (and likely Deimos) resulted from an impact with Mars.

Key Points:
- MGS TES spectra of Phobos have clear, diagnostic spectral features and are most consistent with a mixture of finely particulate basalt and phyllosilicates
- The Tagish Lake carbonaceous chondrite meteorite is a poor mid-IR spectral analog for Phobos
- A basaltic composition for Phobos supports the impact model for Martian moon formation

Correspondence to:
T. D. Glotch,
timothy.glotch@stonybrook.edu

Citation:
Glotch, T. D., Edwards, C. S., Yesiltas, M., Shirley, K. A., McDougall, D. S., Kling, A. M., et al. (2018). MGS-TES spectra suggest a basaltic component in the regolith of Phobos. *Journal of Geophysical Research: Planets*, *123*, 2467–2484. https://doi.org/10.1029/2018JE005647

Received 19 APR 2018
Accepted 23 AUG 2018
Accepted article online 24 SEP 2018
Published online 3 OCT 2018

Author Contributions

Conceptualization: Timothy D. Glotch, Christopher S. Edwards
Formal analysis: Mehmet Yesiltas
Funding acquisition: Timothy D. Glotch
Methodology: Timothy D. Glotch, Christopher S. Edwards, Mehmet Yesiltas, Katherine A. Shirley, Dylan S. McDougall, Alexander M. Kling
Supervision: Timothy D. Glotch
Writing - original draft: Timothy D. Glotch, Christopher S. Edwards, Joshua L. Bandfield, Christopher D. K. Herd
Writing – review & editing: Timothy D. Glotch

1. Introduction

The spectral properties of Phobos have been previously investigated at both visible/near-infrared (VNIR) and midinfrared (MIR) wavelengths (Fraeman et al., 2012, 2014; Giuranna et al., 2011; Murchie et al., 1999; Murchie & Erard, 1996; Pieters et al., 2014; Rivkin et al., 2002). VNIR spectra of Phobos include a weak 2.8 μm metal-OH feature that has been interpreted to be diagnostic of desiccated phyllosilicates or solar wind-induced hydroxylation of the Phobos regolith surface and a broad 0.65-μm feature that may be attributable to Fe-bearing phyllosilicates or Rayleigh scattering by nanophase metallic Fe particles (Fraeman et al., 2014). Giuranna et al. (2011) identified a number of features in mid-IR Mars Global Surveyor Thermal Emission Spectrometer (MGS-TES) and Mars Express Planetary Fourier Spectrometer data that they suggested are consistent with the presence of phyllosilicates and a highly feldspathic surface.

In this work, we reevaluate MIR spectra of Phobos acquired by the MGS-TES experiment. We remapped the TES detector footprints onto the surface of Phobos to provide an accurate geographic distribution of spectral signatures. In addition, we acquired ambient VNIR and simulated Phobos environment (SPE) MIR spectra of a

Table 1
Unique Identifiers (ICK and Detector Number) and Derived Bolometric Surface Temperature for Each TES Spectrum Used in This Study

Ick	Det.	*T* (K)	Ick	Det.	*T* (K)	Ick	Det.	*T* (K)	Ick	Det.	*T* (K)
2373	2	283.9	2402	2	283.6	2422	3	257.9	2428	1	288.2
2373	3	273.2	2402	3	257.1	2423	1	287.6	2428	2	262.8
2374	2	293.8	2402	4	292.7	2423	2	261.2	2428	3	263.2
2374	5	266.1	2402	5	281.5	2423	3	260.2	2429	1	285.9
2374	6	256.9	2402	6	274.3	2424	1	289.4	2429	2	260.9
2375	5	286.5	2418	1	250.5	2424	2	262.8	2429	3	261.7
2375	6	273.1	2419	1	262.2	2424	3	262.0	2430	1	281.9
2398	1	275.2	2419	2	251.2	2425	1	290.1	2430	2	258.3
2399	1	296.3	2420	1	272.4	2425	2	264.1	2430	3	259.1
2399	2	273.3	2420	2	253.8	2425	3	263.5	2431	1	276.1
2399	3	265.2	2420	3	254.9	2426	1	290.0	2431	2	255.2
2400	2	285.8	2421	1	279.2	2426	2	264.6	2431	3	257.7
2400	3	277.7	2421	2	256.1	2426	3	264.5	2432	1	267.7
2400	4	269.4	2421	3	256.5	2427	1	289.5	2432	2	252.2
2400	5	253.3	2422	1	284.4	2427	2	264.0	2432	3	255.9
2401	5	266.9	2422	2	258.6	2427	3	264.3	2433	1	256.9
2401	6	261.4									

purported meteorite analog (Tagish Lake; e.g., Brown et al., 2000; Hiroi et al., 2001; Rosenblatt, 2011), as well as basalt and natural and thermally desiccated nontronite to represent potential spectroscopic components of Martian and/or meteoritic origin. Although the TES footprints cover a limited surface area on Phobos, we find that the data are broadly consistent with the presence of a finely particulate, low thermal inertia (less than a few tens of microns; Weschler et al., 1972) darkened basalt, perhaps with the admixture of phyllosilicate or other constituents. These results are generally inconsistent with the hypothesis that Phobos is a captured carbonaceous asteroid (Murchie et al., 1999; Pajola et al., 2012, 2013; Pang et al., 1978; Pollack et al., 1978; Rivkin et al., 2002). On the other hand, the presence of a basaltic component in the regolith supports the hypothesis that Phobos (and Deimos) formed as a result of a large impact with Mars (Canup & Salmon, 2018; Craddock, 2011; Hyodo et al., 2017; Rosenblatt & Charnoz, 2012). The presence of multiple identifiable spectral features in the TES spectra of Phobos suggests that mid-IR spectroscopy is a useful tool to study the composition of airless bodies, especially those for which VNIR spectra are largely dark and featureless.

2. Samples and Methods

2.1. TES Data Processing

We gathered TES spectra from four early mission MGS aerobraking orbits (orbits 476, 501, 526, and 551) and subsequently culled the data to include only the highest-temperature daytime observations (>240 K) of the Phobos surface to maximize the signal-to-noise ratio of the data. The data were further restricted to only include spectra where the TES field of view was calculated to be completely on the Phobos disk, without any contribution from space. We find that the only spectra meeting these criteria were acquired during orbit 551. These are used exclusively for our analysis. A total of 65 spectra were chosen with bolometric temperatures >240 K. This temperature cutoff provides relatively high signal-to-noise ratio spectra while still providing an adequate number of spectra with good geographical coverage of Phobos for our analysis. The unique identifiers (ICK—incremental counter keeper—and detector) and derived bolometric temperature for each observation used in this study are listed in Table 1.

The standard geometric processing available for TES data is not appropriate for spectra acquired of Phobos because of the relatively large footprint relative to the size of the body. As such we developed a processing routine to determine the shapes of the footprints of the 3 × 2 array of TES detectors. This routine utilized a custom set of Navigation and Ancillary Information Facility (NAIF) NAIF SPICE routines that account for spacecraft position, orientation, and the positions of the various bodies under consideration (e.g., Mars and Phobos). We did not use a shape model for Phobos but instead assumed a triaxial ellipsoid. While a shape

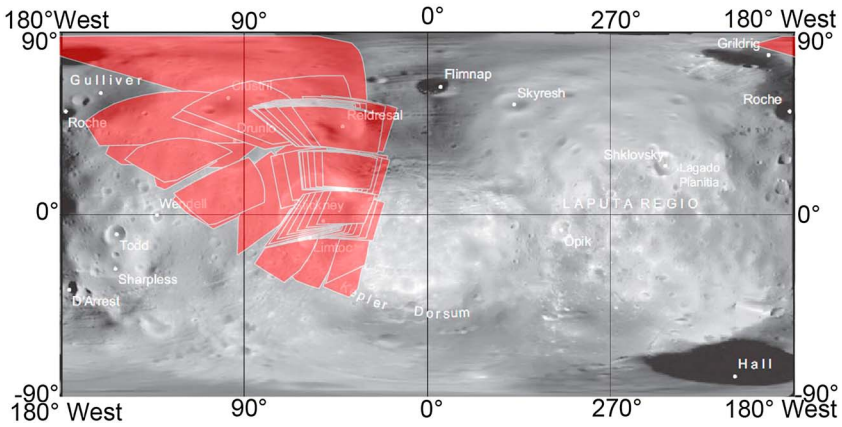

Figure 1. Coverage map of high-quality TES spectra from orbit 551 on a Mars Express HRSC global photomosaic (Wälisch et al., 2010).

model (Gaskell, 2011) is available, the use of this shape model to calculate the intersection with the surface was not warranted, given the uncertainty in TES pointing. The large TES footprint and relatively low signal-to-noise ratio of the data set (given low spectral contrast) necessitates the averaging of large areas. This is important for determining the general location of the measurement on the surface, but the specific pixel edge boundaries are less important for this spectral study. We also use the angle of the TES pointing mirror to rotate the viewing geometry vector and account for any spacecraft movement during the instrument integration time (1.8 s) to collect a spectrum. This extended duration without image motion compensation caused smear, which, for a polar orbit such as that used for the TES mapping phases, enlarged the footprint in the along-track direction. In the case of Phobos, the observing geometry was such that the observations had only negligible smear. In order to accurately map the TES footprints to Phobos, we determined the extent of the instantaneous field of view of each individual detector of the 3×2 array. To do so, a 20×20 array of pointing vectors was calculated for each detector, sampling the full field of view. Where these vectors intersected with the Phobos body, the latitude and longitude of the intersection point were stored in a data array. At the completion of this mapping effort we converted the latitude/longitude point array into a polygon following a convex hull method that was later simplified to reduce the number of polygon points (Figure 1). This method remains valid even if the polygon is not fully filled; however, to avoid complications with mixing of temperatures (e.g., space and Phobos), footprints that are not fully filled (even by a single vector) are excluded from our analysis.

An optimized map of the surface coverage of high-quality TES spectra is shown in Figure 1. TES footprints cover Stickney crater and craters Drunlo and Custril and the western portion of the bright grooved terrain east of Stickney and north of Kepler Dorsum. The TES data coverage corresponds primarily with the *blue unit* defined by Murchie and Erard (1996) but also includes portions of the *red unit*. The optimized TES footprint geometry is similar to the pointing defined by Giuranna et al. (2011) but extends farther to the north and west than suggested by that work.

To reduce spectral slopes in the emissivity spectra, it is necessary to account for the wide range of temperatures expected on Phobos within individual TES footprints. Therefore, we modeled the radiance of the surface as a linear combination of blackbodies (Planck radiance). This method uses a nonnegative least squares fitting routine (Rogers & Aharonson, 2008) to identify a maximum of three blackbodies of different temperatures and their appropriate proportions to complete a best fit. For each spectrum, we generated a suite of 70 blackbodies from 100 to 300 K and allowed the unmixing model to identify the minimum suite of blackbodies. In general, we found that only three blackbody curves were needed to achieve a fit that could not be improved with the inclusion of additional blackbodies. Typically, if the model utilized more than three blackbodies, it did so at low ($<$1% contribution) levels. This approach is reasonable for data where the spectral contrast is low, as is the case here. Furthermore, we experimented with limiting the fitting routine over certain spectral ranges (e.g., Christiansen feature and long-wavelength tail) and found no significant differences in the fitting of Planck functions. Because the least squares fit of multiple blackbodies can result in values

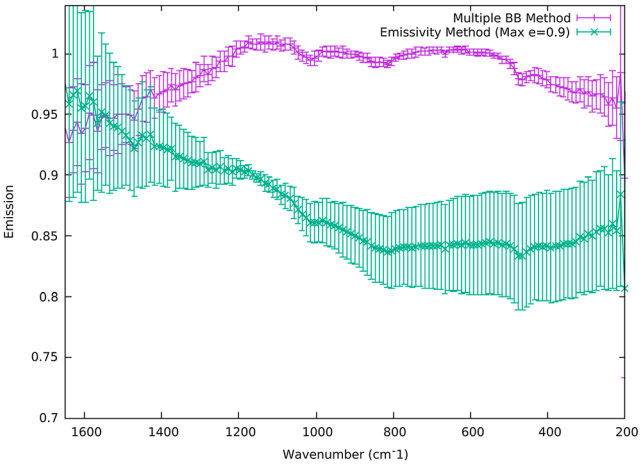

Figure 2. Average TES spectra of Phobos derived using the multiple blackbody methods (purple) and the traditional single temperature method (green). Error bars represent the 1-sigma standard deviation for each spectrum.

greater than unity at some wavelengths, the resulting spectra are not strictly emissivity, and we report the values as *emission* or *thermal emission*. However, conversion of these data to standard emissivity following the methods of Christensen et al. (2001) is also possible, though it requires the assumption of an emissivity maximum less than unity (in this case we choose 0.9 near 1,200 cm^{-1}). Using a single temperature and assuming a maximum emissivity <1 generally results in significant spectral slopes (Figure 2) that are more severe than those present in the spectra computed from the multiple blackbody fitting routine. As such, we elect to use the multiple blackbody routine for our spectral comparisons despite the minor nonphysical aspects. For example, these spectra occasionally have values greater than unity but are not affected by strong spectral slopes due to surface anisothermality.

2.2. Samples

2.2.1. Tagish Lake Sample and Characterization

A 0.23-g sample of the Tagish Lake (C2-ungrouped) meteorite was provided from the University of Alberta Meteorite Collection (specimen MET11611/P-1/2/2). The chip was removed from specimen 1 (*TL1*) using a sterile scalpel in a cold glovebox within the Subzero Curation Facility for Astromaterials at the University of Alberta (Herd et al., 2016). Tagish Lake specimens show varying degrees of aqueous alteration, as indicated by petrologic and organic characteristics (Blinova et al., 2014; Herd et al., 2011; Hilts et al., 2014). Although not fully characterized petrologically, specimen TL1 is similar in many respects to specimen TL5B of previous studies (Simkus, 2017). Since TL5b is among the least altered lithologies (e.g., Blinova et al., 2014), we infer that TL1 is similar and reflects a portion of the Tagish Lake parent body that saw a relatively low degree of aqueous alteration. The sample as provided was an intact but friable chip. Subsequent to acquiring spectra of the intact chip, we acquired additional spectra of the sample after gently crushing it into a coarse particulate (~250–500 μm) and then a fine powder (Figure 3).

Prior to crushing the sample, we characterized it using micro-Raman spectroscopy to determine the presence of phases in the sample. We acquired micro-Raman spectra using a WiTEC alpha300R confocal Raman imaging system in the Stony Brook University Center for Planetary Exploration equipped with a 532-nm Nd:YAG laser, spectrometer with a CCD-camera (peltier cooled to −60 °C), and 50× objective (NA = 0.8), resulting in a spot size at the sample surface of ~0.8 μm. The laser power on the sample surface was kept between 0.2 and 2.4 mW measured at the objective to avoid thermal alteration of the samples.

As expected, the spectra (Figure 4) exhibit near-ubiquitous carbon along with magnetite, olivine, troilite, metal oxide, Ca (OH) apatite, and an unidentified sulfide. Phase identifications were made by comparing

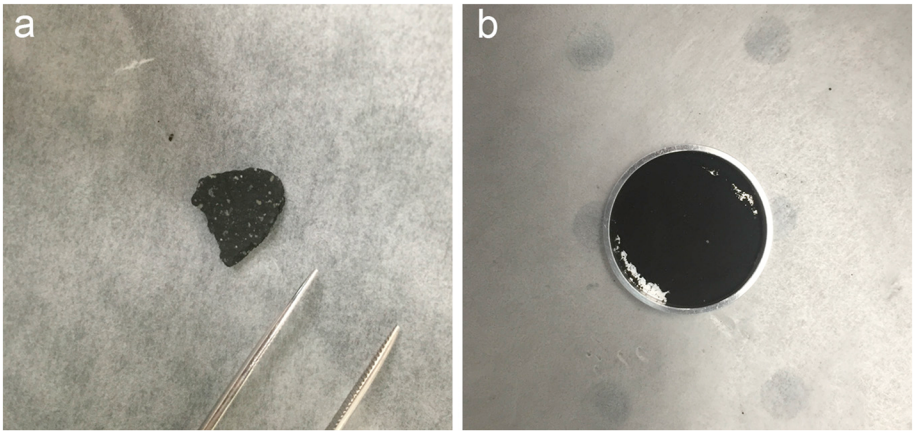

Figure 3. Images of the (a) in-tact chip of Tagish Lake provided for this study (tweezers for scale) and (b) the finely crushed sample in the sample cup for thermal IR measurements in PARSEC.

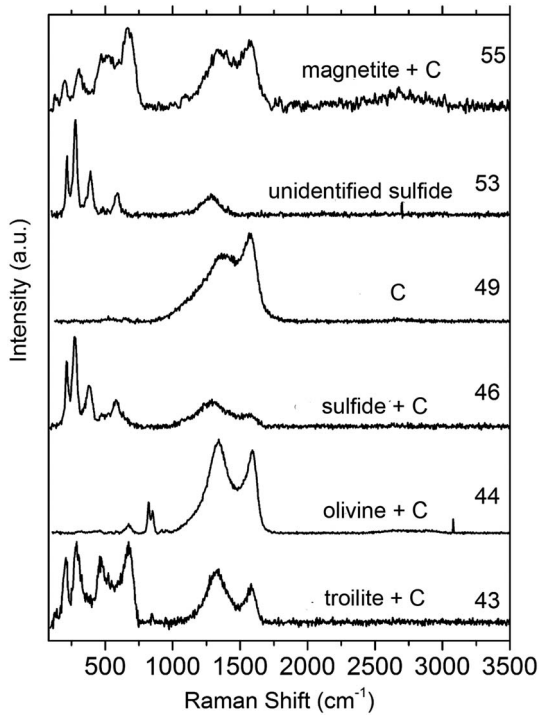

Figure 4. Representative micro-Raman spectra of major phases present in the Tagish Lake sample used for this study. Numbers next to each spectrum indicate the number of points that the phase was found in during analysis.

our spectra with the RRUFF database using the CrystalSleuth software available at http://rruff.info/about/about_download.php. Apatite is not common in Tagish Lake, and the identification is based on the presence of a single peak above the level of the noise at ~961 Δ cm^{-1}. The lack of phyllosilicate detection in Raman spectra, which would be expected for Tagish Lake based on its known mineralogy, may be due to their poorly crystalline nature and/or interlayering with magnetite.

2.2.2. Basalt and Nontronite Samples

A sample of Columbia River basalt was provided by J. A. Hurowitz for use in this study. It was collected at the Lawyer Canyon site in western Idaho and has a relatively low level of chemical weathering (chemical index of alteration ~40). The sample was provided as a <45-μm size fraction. We crushed and isolated the <10-μm size fraction in ethanol using Stokes' settling method (Day, 1965; Gee & Bauder, 1986; Salemi et al., 2010). Details of the sample chemistry and mineralogy are provided in Thomson et al. (2014).

A <10-μm size fraction of the Clay Minerals Society source clay NAu-2 nontronite was prepared by grinding and settling using the same procedure described above. Following the methods of Che et al. (2011), a portion of the the nontronite was thermally altered at 700 °C under ambient atmospheric conditions in a furnace to simulate impact shock/desiccation processes.

Because visible albedo has a strong effect on mid-IR emissivity spectra acquired in an airless body environment (Shirley et al., 2018), we darkened portions of the nontronite, thermally altered nontronite, and basalt with nanophase carbon lamp black (90-nm average particle size), until carbon was 5 wt.% of the each sample. Addition of the carbon resulted in albedos (measured at 750 nm) of 0.059, 0.055, and 0.042 for the basalt, thermally altered nontronite, and nontronite, respectively. We note here that the use of carbon to darken the samples is not intended as a realistic analog of Phobos' surface. Rather, we use it as a proxy for any process that could reduce the albedo of a surface, including space weathering, impact shock/shock melting, and/or the presence of actual carbonaceous material.

2.3. PARSEC Description and MIR Data Acquisition

To provide direct comparisons of the Tagish Lake, basalt, and clay samples to TES spectra of Phobos, we must acquire spectra in a simulated airless body environment. The vacuum environment of space results in a steep thermal gradient (up to 40 K per 100 μm on the Moon) in the upper regolith of airless planetary surfaces (Henderson & Jakosky, 1994, 1997; Logan & Hunt, 1970). This thermal gradient results in the convolution of multiple temperatures in each thermal infrared measurement, which complicates interpretations of the spectra. To address this, we use the Planetary and Asteroid Regolith Spectroscopy Environmental Chamber (PARSEC) in the Center for Planetary Exploration at Stony Brook University (Figure 5). PARSEC is designed to measure up to six samples per measurement session under environmental conditions of airless planetary bodies (e.g., Phobos, asteroids, and the Moon). The Tagish Lake samples (chip, coarse ground, and finely ground preparations) were measured under terrestrial ambient conditions (AMB) and then under SPE conditions. AMB spectra were acquired at 1,000-mbar pressure, with the chamber temperature at ~300 K, the sample temperature at 350 K, and with no illumination.

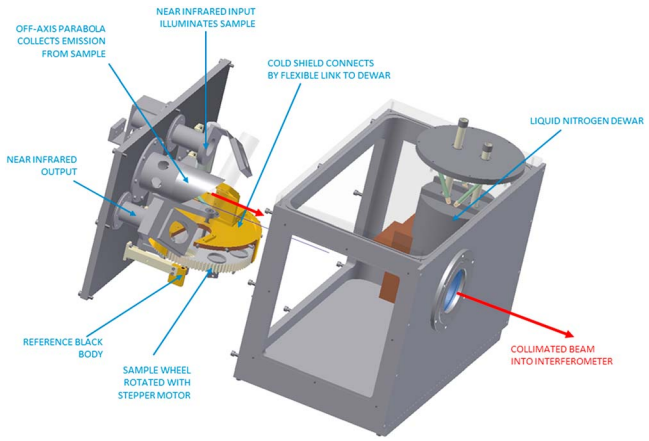

Figure 5. Major components of the Planetary and Asteroid Regolith Spectroscopy Environmental Chamber (PARSEC) used to collect simulated Phobos environment MIR spectra.

We simulate the Phobos environment by pumping the PARSEC chamber down to a pressure of <10^{-5} mbar, heating the samples from below to 350 K, heating from above via 75-W quartz halogen lamp connected to a tunable power source, and cooling the chamber to <150 K. Depending

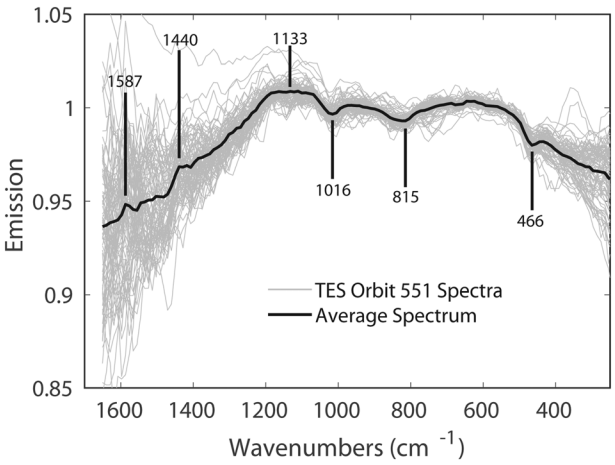

Figure 6. TES spectra used in this study and their average. The average spectrum has clearly defined minima at 1,016, 815, and 466 cm^{-1}, a broad CF centered at 1,133 cm^{-1}, and weaker maxima at 1,440 and 1,587 cm^{-1}.

on the power source settings, our maximum sample brightness temperatures ranged from ~365 to 420 K, which is considerably warmer than the measured bolometric temperatures measured by TES at Phobos (Table 1). However, this variability in maximum brightness temperature has a negligible effect on the calculated emissivity (see section 4). The PARSEC cold shield is actively cooled via input of liquid nitrogen into an internal dewar, and pressure is controlled by a Pfeiffer HiCube turbo vacuum pump. PARSEC is connected to a Nicolet 6700 Fourier transform infrared (FTIR) spectrometer equipped with a KBr beamsplitter and a deuterated L-alanine doped triglycine sulfate (DLaTGS) detector with a KBr window, measuring thermal emission across 400–2,200 cm^{-1} with a resolution of 4 cm^{-1}. The spectrometer is actively purged with air scrubbed of CO_2 and water vapor. Measurements of a black body target in PARSEC are acquired at 340 and 370 K at the beginning of each series of measurements for use in calibration.

The emissivity spectra acquired in PARSEC display characteristic Reststrahlen bands, transparency features, and the Christiansen feature (CF) emissivity maximum. The Reststrahlen bands generally occur between ~1,100 and 400 cm^{-1} and are the result of stretching and bending vibrational modes and are thus characteristic of mineral composition (Conel, 1969; Lyon, 1964). Transparency features occur when the particle size is on the order of the wavelength of light or smaller and result from multiple scattering of light by the particulates (e.g., Cooper et al., 2002). The CF is an emissivity maximum that occurs where the imaginary index of refraction (k) is close to zero and the real index (n) approaches that of the surrounding medium. In silicates, its position is related to the polymerization of silica tetrahedra and is thus diagnostic of composition (Conel, 1969; Logan et al., 1973).

2.4. VNIR Data Acquisition

VNIR bidirectional reflectance spectra (350–2,500 nm) were collected on an ASD Fieldspec3 Max spectroradiometer with incidence and emergence angles of 30° and 0° respectively at the Stony Brook University Center for Planetary Exploration. The gain and offset of the detectors were optimized using a calibrated Spectralon standard prior to acquisition of spectra. Spectra were acquired in a dark room behind a closed shroud to minimize the effects of stray light. Spectra were referenced to a calibrated Spectralon standard, splice corrected, and processed to absolute reflectance. A total of 200 scans were averaged for each sample, and 400 scans were averaged for the Spectralon target.

3. Results

3.1. TES Data Analysis

The TES spectra used in this study and their average are shown in Figure 6. From the center of the CF emission maximum to lower frequencies (longer wavelengths), the spectra define a tight range, with clear thermal emission minima at 1,016, 815, and 466 cm^{-1} (9.84, 12.27, and 21.46 μm). The CF is broad and centered at 1,133 cm^{-1} (8.83 μm). At higher frequencies (shorter wavelengths) than the CF, the spectra are noisier and have a larger range of thermal emission values. Still, the average shows weak maxima centered at 1,440 and 1587 cm^{-1} (6.94 and 6.30 μm).

The majority of spectra used for this study fall on and around Stickney crater, in the *bluer* unit defined by Murchie and Erard (1996), although some relatively large footprints fall on the *red* unit. We investigated the spectral differences between the blue and red units by manually separating the spectra into those categories (Figure 7). There is some unavoidable overlap between the two groups, and some of the red spectra likely contain small amounts of ejecta from the crater. Regardless, this exercise allows us to search for differences between the surface Phobos regolith and deeper material excavated by Stickney.

Between ~1,200 and 250 cm^{-1}, there is remarkably little difference between the averages of the blue and red unit spectra (Figure 8). The major emission minima defined in the average spectrum (Figure 6) are present in the averages of both subsets of spectra. The major differences between the spectra are seen at the CF and higher frequencies. The blue average spectrum has a clear CF maximum at 1,132 cm^{-1} (8.83 μm), whereas

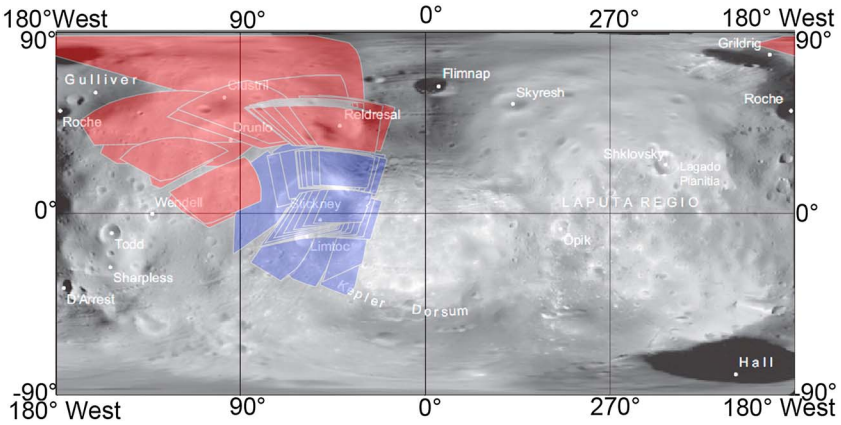

Figure 7. Distribution of TES footprints covering the Phobos red and blue units defined by Murchie and Erard (1996).

the off-Stickney average spectrum has more of a CF doublet, with a longer maximum at 1,090 cm^{-1} (9.17 μm) and a shorter maximum at 1,164 cm^{-1} (8.59 μm).

At higher frequencies than the CF, the spectra diverge substantially, with the red unit average having a more clearly defined minimum at ~1,520 cm^{-1} and a maximum at 1,587 cm^{-1}. However, given the similarities at lower frequencies and the substantial scatter in individual spectra at higher frequencies (Figure 6), we cannot confidently state that the two average spectra are substantially different.

3.2. Simulated Phobos Environment MIR Spectra

Ambient and SPE spectra of each of the three preparations of Tagish Lake are shown in Figure 9. In general, there are only minor differences between the ambient and SPE spectra of the Tagish lake chip. Both spectra have a doublet in the CF region with maxima centered at 1,186 and 1,124 cm^{-1} (8.43 and 8.89 μm) and minima centered at 873, 567, and 416 cm^{-1} (11.45, 17.64, and 24.04 μm). The ambient spectrum has larger spectral contrast at the lowest frequencies.

The AMB and SPE spectra of the ground material differ substantially from each other and from the spectrum of the chip. The ambient spectrum of the coarse ground sample has a CF maximum at ~1,117 cm^{-1} (8.95 μm) with weak minima centered at 1,022 and 887 cm^{-1} (9.78 and 11.27 μm). The SPE spectrum has a CF maximum at 1,080 cm^{-1} (9.26 μm) and comparatively weaker minima centered at 1,022 and 887 cm^{-1}. At lower frequencies, the spectra are essentially featureless, characterized by a broad, weak hump. The SPE spectrum also includes a weak, broad minimum centered at 1,348 cm^{-1} (7.42 μm) that is absent in the ambient spectrum.

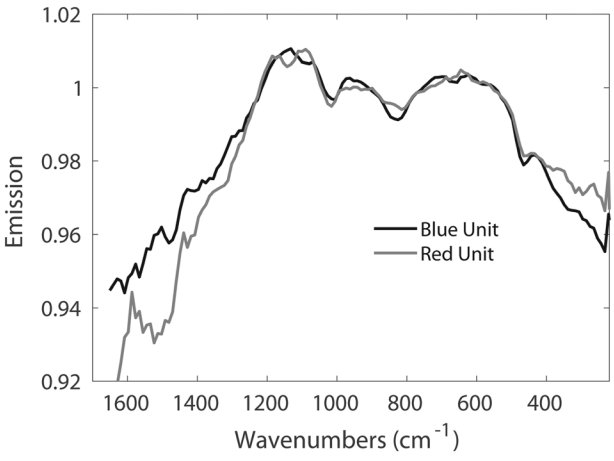

Figure 8. Averages of TES spectra from the red and blue units defined by Murchie and Erard (1996).

The ambient spectrum of the fines has a CF emissivity maximum at 1,097 cm^{-1} (9.12 μm) with weak minima centered at ~1,335 and 874 cm^{-1} (7.49 and 11.44 μm). By contrast, the SPE spectrum has a broad CF emissivity maximum centered at ~1,030 cm^{-1} (9.71 μm) with strong minima centered at ~1,323 and 815 cm^{-1} (7.56 and 12.27 μm). A shoulder feature is present at wavelengths just shortward of the CF at ~1,169 cm^{-1} (8.55 μm), and additional weak minima are present at 894 and 551 cm^{-1} (11.19 and 18.15 μm).

Overall, the ambient spectra of Tagish Lake contain few distinguishing features other than the CF, except for the spectrum of the intact chip, which has several strong, diagnostic features that match the spectral features of magnetite and olivine and are consistent with our Raman observations (Figure 9). Sulfides are generally featureless between 2,000 and ~600 cm^{-1} and may also account for the steep dropoff in emissivity from 600 to 400 cm^{-1}. Strong absorptions near ~1,000 cm^{-1} due to phyllosilicates might be expected based on the reported mineralogy (e.g., Zolensky et al., 2002) and previous infrared spectra (Izawa et al., 2010;

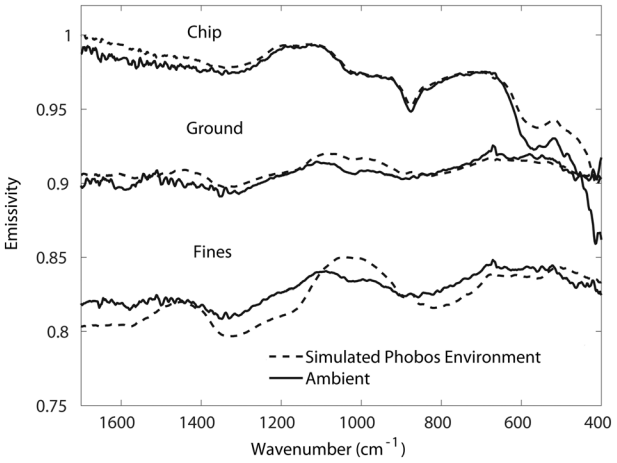

Figure 9. Ambient and simulated Phobos environment spectra of Tagish Lake prepared as an in-tact chip, coarse particulates, and fine particulates. Spectra are offset for clarity.

Matrajt et al., 2004; Osawa et al., 2005) of Tagish Lake, but they are absent in the spectrum.

Ambient and SPE spectra of basalt are shown in Figure 10. The ambient spectrum of finely particulate basalt (Figure 10a) has a CF emissivity maximum at 1,178 cm^{-1} (8.49 μm) and a major emissivity minimum at 833 cm^{-1} (12.00 μm). Weak minima also occur at 1,092, 1,024, 995, 927, 565, and 488 cm^{-1} (9.15, 9.77, 10.05, 10.79, 17.70, and 20.49 μm). At wavelengths shortward of the CF, the spectrum exhibits the typical drop in emissivity characteristic of finely particulate silicates. Peaks at 1,377, 1,454, and 1,601 cm^{-1} (7.26, 6.88, and 6.25 μm) may indicate the presence of minor carbonate and hydrated alteration phases. The emissivity minimum in the Reststrahlen/transparency feature region is 0.969 at 833 cm^{-1}.

The ambient spectrum of darkened basalt (Figure 10a) has much reduced spectral contrast compared to the undarkened spectrum, with a minimum emissivity in the Reststrahlen/transparency region of 0.986 at 833 cm^{-1}. Minor minima present in the undarkened spectrum are also present in the darkened spectrum, but with reduced spectral contrast. It is difficult to pinpoint a CF position in the darkened spectrum, which does not exhibit a strong reduction in emissivity at high frequencies but instead has a broad, shallow curvature centered at ~1,273 cm^{-1} (7.86 μm). The spectrum also does not exhibit any emissivity maxima due to hydration or carbonates at high frequencies.

The SPE spectrum of finely particulate basalt (Figure 10b) has a CF emissivity maximum at 1,194 cm^{-1} (8.38 μm) and a major emissivity minimum at 829 cm^{-1} (12.06 μm). Weak minima also occur at 1,092, 1,012, and 700 cm^{-1} (9.16, 9.88, and 14.29 μm). At wavelengths shortward of the CF, the spectrum has a strong drop in emissivity, with peaks at 1,454 and 1,600 cm^{-1} (6.88 and 6.25 μm). The minimum emissivity in the Reststrahlen/transparency feature region is 0.973 at 829 cm^{-1}.

The SPE spectrum of darkened basalt (Figure 10b) stands in sharp contrast to the undarkened spectrum. The CF shifts to 1,155 cm^{-1} (8.66 μm), and the spectral contrast is greatly reduced, with a minimum emissivity of 0.986 at 829 cm^{-1}. The major emissivity minimum is present at 829 cm^{-1}, with additional minor features at the same frequencies seen for the undarkened basalt. At wavelengths shortward of the CF, the spectrum displays a shallow, nearly featureless slope, in which the carbonate and hydration bands are greatly reduced in strength.

Ambient and SPE spectra of nontronite and thermally altered nontronite are shown in Figure 11. The ambient and darkened spectra of nontronite exhibit a variety of features in common (Figure 11a), including a CF emissivity maximum at 1,240 cm^{-1} (8.06 μm) and emissivity minima at 1,134, 1,078, 903, 812, 766, 507, and 436 cm^{-1} (8.82, 9.28, 11.07, 12.32, 13.05, 19.72, and 22.94 μm). In all cases, the major emissivity minima are shallower for the darkened spectrum, with a minimum emissivity in the Reststrahlen/transparency band region of 0.913 for the nontronite and 0.979 for the darkened nontronite. In several cases, especially at

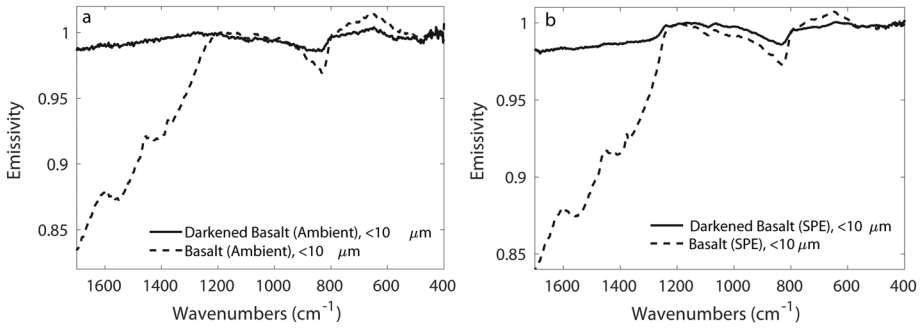

Figure 10. (a) Ambient and (b) simulated Phobos environment spectra of <10-μm basalt and <10-μm basalt darkened with 5 wt.% carbon black.

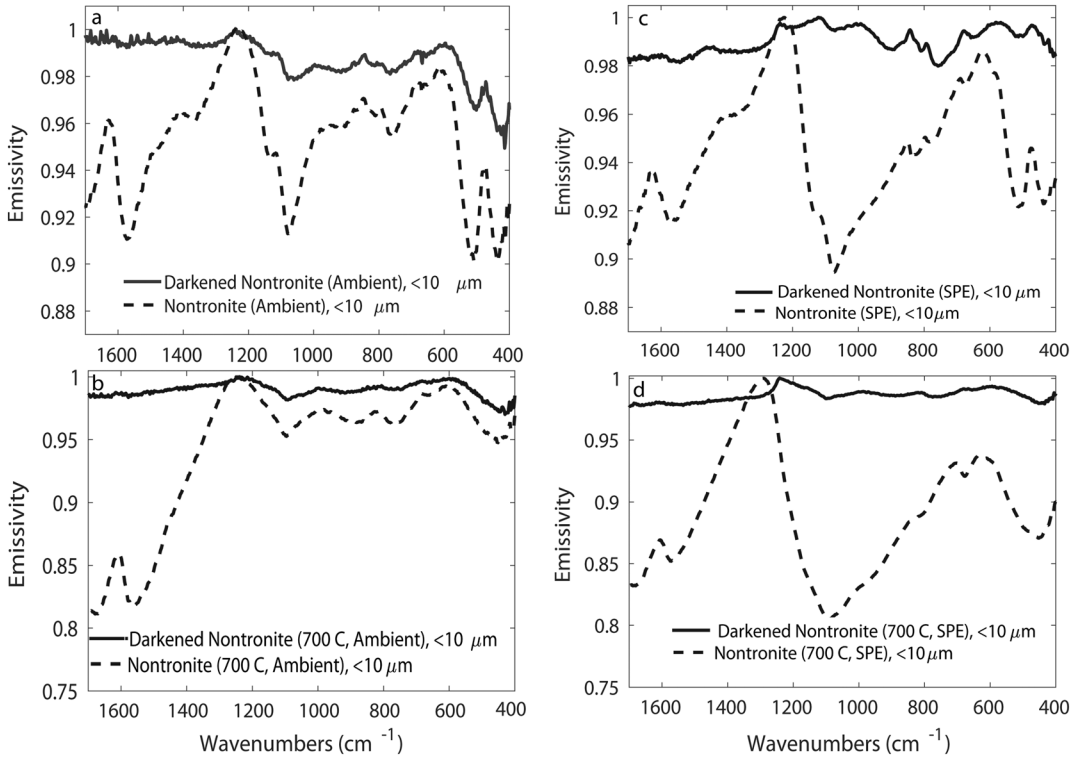

Figure 11. Ambient (a, b) and simulated Phobos environment (c, d) spectra of nontronite and thermally altered nontronite. (a) Ambient nontronite (<10 μm) and darkened nontronite (5 wt.% carbon). (b) Ambient nontronite (<10 μm) and darkened thermally altered nontronite (5 wt.% carbon). (c) SPE nontronite (<10 μm) and darkened nontronite (5 wt.% carbon). (d) SPE thermally altered nontronite (<10 μm) and darkened nontronite (5 wt.% carbon).

1,078 cm^{-1}, the bands are slightly broader. The strong decrease in emissivity at frequencies higher than the CF position that is seen in the nontronite spectrum is absent in the darkened nontronite spectrum. The H_2O fundamental emissivity maximum at 1,626 cm^{-1} (6.15 μm) in the nontronite spectrum is also absent in the darkened nontronite spectrum.

Ambient spectra of thermally altered nontronite (Figure 11b) also exhibit similar CF and Reststrahlen/transparency band positions, with a CF position at 1,238 cm^{-1} (8.08 μm) and emissivity minima at 1,090, 881, 768, and 451 cm^{-1} (9.17, 11.35, 13.02, and 22.17 μm). All bands exhibit shallower spectral contrast for the darkened thermally altered nontronite, and the 881 and 768 cm^{-1} bands exhibit substantial broadening. The minimum emissivity in the Reststrahlen/transparency feature region is 0.952 for the thermally altered nontronite and 0.982 for the darkened thermally altered nontronite. The darkened thermally altered nontronite also has reduced spectral contrast at wavelengths shortward of the CF. The H_2O fundamental emissivity maximum at 1,610 cm^{-1} (6.21 μm) in the thermally altered nontronite spectrum is present, but extremely weak in the darkened spectrum.

The SPE spectrum of nontronite (Figure 11c) displays a CF at 1,225 cm^{-1} (8.16 μm) with a broad minimum centered at 1,072 cm^{-1} (9.33 μm). Superimposed on the broad minimum are local minima at 1,128, 835, 772, and 673 cm^{-1} (8.87, 11.98, 12.95, and 14.86 μm). Additional minima occur at 515 and 436 cm^{-1}. At wavelengths shortward of the CF, this spectrum also exhibits the typical drop in emissivity characteristic of finely particulate silicates. The emissivity maximum at 1,628 cm^{-1} (6.14 μm) is due to structural water in the nontronite. The minimum emissivity in the Reststrahlen/transparency feature region is 0.895 at 1,072 cm^{-1}.

The SPE spectrum of darkened nontronite (Figure 11c), like that of darkened basalt, has a much reduced spectral contrast compared to the undarkened spectrum, with a minimum emissivity of 0.98 at 756 cm^{-1} (13.23 μm). In addition, the CF has shifted from 1,225 to 1,115 cm^{-1} (8.16 to 8.97 μm)

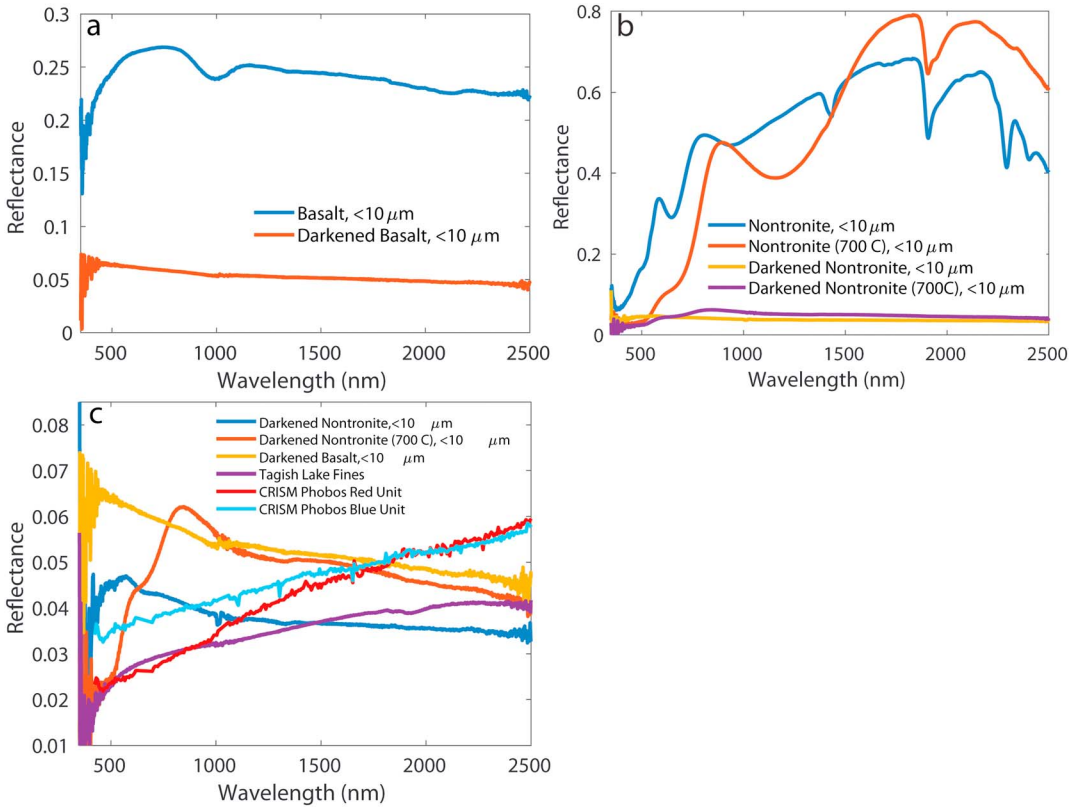

Figure 12. VNIR spectra of <10-μm size fractions of basalt, darkened basalt, nontronite, darkened nontronite, thermally altered nontronite, darkened thermally altered nontronite, and Tagish Lake fines. (a) Basalt and darkened basalt. (b) Nontronite, thermally altered nontronite, and their darkened equivalents. (c) Zoom-in plot of darkened sample spectra with Tagish Lake fines and CRISM spectra of red and blue units.

and the silicate emissivity roll-off at wavelengths shortward of the CF is substantially reduced. The hydration feature at 1,628 cm^{-1} (6.14 μm) seen in the undarkened spectrum is absent. The spectrum includes numerous minima, found at 1,072, 897, 808, 756, 648, 521, and 434 cm^{-1} (9.33, 11.15, 12.38, 13.23, 15.43, 19.19, and 23.04 μm).

The SPE spectrum of thermally altered nontronite (Figure 11d) has a CF emissivity maximum at 1,292 cm^{-1} (7.74 μm) with a broad minimum centered at 1,090 cm^{-1} (9.17 μm). Superimposed on the broad minimum are weak shoulders at ~982 and 822 cm^{-1} (10.18 and 12.17 μm). Additional distinct minima are also present at 677 and 453 cm^{-1} (14.77 and 22.07 μm). At wavelengths shortward of the CF, this spectrum also exhibits the typical drop in emissivity characteristic of finely particulate silicates. The emissivity maximum at 1,606 cm^{-1} (6.23 μm) is due to remaining structural water in the thermally altered nontronite. The minimum emissivity in the Reststrahlen/transparency feature region is 0.80 at 1,090 cm^{-1}.

The SPE spectrum of darkened thermally altered nontronite (Figure 11d) has a much reduced spectral contrast, with an emissivity minimum of 0.983 at 1,090 cm^{-1}. The CF shifts from 1,292 to 1,242 cm^{-1} (7.74 to 8.05 μm). Additional emissivity minima are present at ~895, 766, 656, and 446 cm^{-1} (11.17, 13.05, 15.24, and 22.42 μm). As with the basalt, at wavelengths shortward of the CF, the spectrum displays a shallow, featureless slope toward higher frequencies.

3.3. VNIR Reflectance Spectra

Bidirectional VNIR reflectance spectra of basalt, nontronite, thermally altered nontronite (all both undarkened and darkened), and Tagish Lake fines are displayed in Figure 12, along with Compact Reconnaissance Imaging Spectrometer for Mars (CRISM) spectra of the Phobos red and blue units simulated to have incidence angles of 30° and emergence angles of 0° (Fraeman et al., 2012). The <10-μm basalt sample (Figure 12a) has a maximum

reflectance of 0.268 at 724 nm, with a 1-μm pyroxene electronic transition band centered at 987 nm and a shallow 2-μm band centered at 2,120 nm. The spectrum exhibits a slight blue slope. The darkened basalt sample (Figure 12a) has a low albedo and a blue slope, with the highest reflectance at the shortest wavelengths. The spectrum exhibits high noise at <450 nm and >2,400 nm and near 1,000 nm, at the interface between two detectors. The darkened basalt spectrum exhibits no bands above the level of noise in the spectrum.

The nontronite, thermally altered nontronite, and their darkened equivalents are displayed in Figure 12b. Nontronite has a maximum reflectance of 0.683 at 1,831 nm. It exhibits an overtone of the OH stretching mode centered at 1,432 nm, combination modes of H_2O at 1,908 nm, and combinations of OH-stretching and metal-OH bending modes at 2,293 and 2,404 nm. It also exhibits crystal field electronic transitions centered at 933 and 647 nm, with a shoulder at ~507 nm.

The thermally altered nontronite has a higher overall albedo, with a maximum reflectance of 0.7902 at 1,841 nm. It has completely lost its 1,432-nm H_2O mode, and its metal-OH/OH-stretching combination modes are greatly reduced in strength. The H_2O combination modes at 1,908 nm are still present but reduced in band strength compared to the unheated sample. The spectrum also includes a new broad, deep crystal field band centered at 1,155 nm. The 647-nm crystal field absorption is reduced in strength and better described as a shoulder in the heated nontronite spectrum.

The darkened nontronite and spectrum has a maximum albedo of 0.047 at 573 nm, a slight blue slope over the entire spectral range, and a weak shoulder feature (~0.002 band depth) at 655 nm. An artifact near the detector join is seen at 1,009 nm, but no other features with >0.001 band depths are found. The darkened altered nontronite spectrum is a bit brighter, with a maximum reflectance of 0.062 at 841 nm and a blue slope from that maximum toward longer wavelengths. It has a shoulder feature at ~662 nm and a broad, shallow absorption (~0.01 reflectance) centered at ~1,180 nm.

The Tagish Lake fines spectrum (Figure 12c) is the overall darkest sample, with a maximum reflectance of 0.041 at 2,251 nm and a red slope over the entire spectral range, similar to the slopes seen for the Phobos red and blue units. The spectrum includes very weak absorptions (~0.002 reflectance) centered at ~1,752, 1,844, and 1,918, suggesting the presence of an unknown hydrated phase.

4. Discussion

4.1. Tagish Lake as a VNIR Analog of Phobos

Tagish Lake has been suggested as a compositional analog to D-class asteroids and Phobos based on its low albedo, red slope, and relatively featureless spectrum at VNIR wavelengths (Hiroi et al., 2001; Lynch et al., 2007; Murchie & Erard, 1996; Pajola et al., 2013; Rivkin et al., 2002). Of the VNIR spectra measured in this work, that of Tagish Lake (Figure 12c) is, indeed, the best match to published spectra of Phobos (e.g., Fraeman et al., 2012, 2014; Murchie & Erard, 1996; Rivkin et al., 2002). It has a low albedo, a red slope, and only three very weak spectral features near ~1.9 μm. The other darkened samples all have low albedos but display blue, rather than red, slopes. The darkened basalt and nontronite samples are mostly featureless, with the exception of a ~650-nm feature in the nontronite spectrum that has been observed in CRISM spectra of the Phobos red unit (Fraeman et al., 2014). The darkened thermally altered nontronite spectrum has a strong red slope shortward of ~840 nm that is not seen in Phobos spectra. It should be noted, however, that the nontronite sample was heated in air, under oxidizing conditions. Thermal alteration under reducing vacuum conditions may result in substantial differences to the VNIR and/or MIR spectra.

The blue slopes in the darkened basalt and nontronite spectra are likely a function of the large carbon particle size used to darken the samples (90 nm), which falls above the size (< ~50 nm) at which nanophase absorbers contribute reddening to the spectra (e.g., Lucey & Riner, 2011). Thus, while the blue slopes of these samples make for imperfect VNIR spectra analogs to Phobos, the presence of finely particulate basalt and/or nontronite on the surface of Phobos should not be discounted based on the slopes of these spectra.

4.2. Comparison Between TES and Tagish Lake

Despite the similarities between Tagish Lake and Phobos at VNIR wavelengths, there are substantial differences between the Tagish Lake and Phobos spectra at TIR wavelengths (Figure 13).The closest match between the Tagish Lake and Phobos infrared spectra is for the intact chip. The Phobos and Tagish Lake

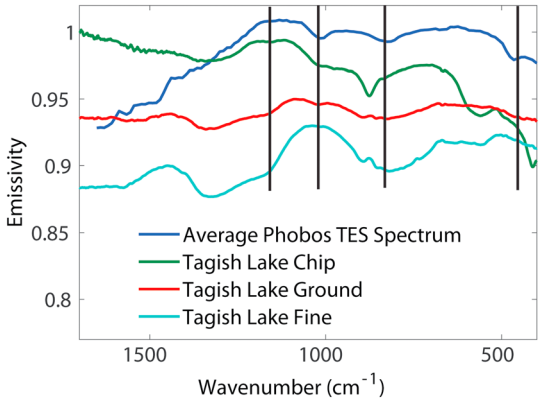

Figure 13. Thermal emission spectra of Phobos and three preparations of the Tagish Lake sample. Vertical lines at 1,133, 1,016, 815, and 466 cm^{-1} show the positions of major spectral features in the Phobos spectrum. Spectra are offset for clarity.

chip spectra both have broad CF maxima, with roughly similar CF positions. In addition, both spectra have minima in the ~1,200–600 cm^{-1} region, although they do not occur at similar positions. In addition, the Tagish Lake spectrum has much deeper emissivity at the longest wavelengths, consistent with the presence of substantial magnetite and sulfide in the sample. While there are some similarities, there are numerous substantial differences, indicating that Tagish Lake (or at least the lithology of Tagish Lake used in this work) is not an appropriate compositional analog for Phobos. Despite the similarities in CF position, the other major spectral features are not good matches. In addition, thermal modeling of Phobos (Lunine et al., 1982; Smith et al., 2018) suggests an average thermal inertia of ~25–80 J · m^2 · K · s$^{1/2}$, consistent with the presence of a fine regolith (likely a few tens of microns; Weschler et al., 1972). However, relating thermal inertia to particle sizes on airless bodies is notoriously difficult (Presley & Christensen, 1997; Weschler et al., 1972) due to grain angularity, roughness, difficulty in deriving accurate thermal inertia values, etc., and as such, we use the thermal inertia constraints listed above as an indicator for fine-grained particles, rather than attempting to derive robust particle sizes. The interpretation of a finely particulate regolith is also supported by the steep dropoff in emissivity of the Phobos spectrum at wavelengths shortward of the CF.

The Phobos spectral character and derived thermal inertia (Lunine et al., 1982; Smith et al., 2018) therefore point to a fine particulate material as the best potential analog to the Phobos spectrum. However, both the coarsely ground and finely particulate Tagish Lake sample preparations differ substantially from the Phobos spectrum. As the particle size decreases from chip to coarse particulates to fine particulates, the CF changes shape and shifts to longer wavelengths. The sharp emissivity minimum at ~867 cm^{-1} disappears and is replaced by a broad transparency feature.

It is unlikely that differences between the Phobos environment and the simulated airless body environment in the PARSEC chamber are the cause of the spectral differences seen in Figure 13. Exposure to the space environment has led to space weathering of Phobos' surface. Space weathering has been shown to alter the mid-IR spectral features of the Moon (Glotch et al., 2015; Lucey et al., 2017), likely the result of an altered thermal gradient caused by reduced visible albedo associated with optically mature surfaces. Space weathering results in a shift of the CF to longer wavelengths and a reduction in Reststrahlen band and transparency feature strength throughout the mid-IR (Glotch et al., 2015; Lucey et al., 2017; Shirley et al., 2018). As seen in Figure 13, the positions of the coarse and finely ground Tagish Lake CF maxima are at much longer wavelengths than that of the Phobos spectrum. The average Phobos spectrum is composed of spectra covering both the Phobos blue and red defined by Murchie and Erard (1996). However, the generally low albedos, flat-to-red slopes, and lack of strong spectral features throughout the VNIR suggest that both the red and blue units could have experienced significant space weathering. Therefore, it is unlikely that the differences between the Phobos spectrum and the Tagish Lake particulate spectra are the result of space weathering.

A possible source of some of the mismatch between the spectra could be due to differences in the thermal gradient in our particulate spectra acquired in the PARSEC chamber compared to that found in the Phobos regolith. In general, our spectra have brightness temperatures that are higher than the bolometric temperatures of Phobos measured by TES (~250–300 K), which are difficult to achieve in PARSEC. To test the effects of brightness temperature on derived thermal emission spectra, we measured the Tagish Lake fine particulate sample over a range of brightness temperatures (322–369 K) achieved by varying the brightness of the solar lamp shining on the sample. Brightness temperature and derived thermal emission spectra are shown in Figure 14. Brightness temperature spectra (Figure 14a) all show the same basic shape, although they are offset by ~10 K each. Emission spectra derived from the brightness temperature spectra (Figure 14b) all have the same shape, with warmer spectra displaying slightly increased spectral contrast compared to the colder spectra. The spectra are nearly identical near the CF (within the level of noise) and at the longest wavelengths. The maximum emissivity difference between the hottest and coldest spectra is only ~0.003 in the transparency feature region and increases steadily at the wavelengths shortward of the CF to a maximum of ~0.012 near the edge of the reliable range of our measurements. We conclude from these data that the regolith

temperature differences between Phobos and the Tagish Lake particulates measured in PARSEC are not likely to be responsible for the spectral differences observed in Figure 13. Therefore, the primary cause of the mid-IR spectral differences between Tagish Lake and Phobos must be due to differences in composition.

4.3. Implications for Composition and Origin of Phobos

The fact that Tagish Lake is a poor mid-IR spectral analog for Phobos calls into question whether D-class asteroids are suitable compositional analogs for Phobos. The conclusion that Tagish Lake is a poor analog for Phobos is supported by telescopic mid-IR emissivity spectra of D-type Trojan asteroids (Emery et al., 2006), which are dissimilar to both Tagish Lake and Phobos. Spectra of other classes of carbonaceous chondrite meteorites, including Allende (CV3) and Murchison (CM2), acquired under similar airless body conditions also appear to be poor matches to the Phobos spectrum (Donaldson Hanna et al., 2017). These spectra have one or more broad, deep features between 400 and 1,000 cm^{-1} that are wholly absent from the average Phobos TES spectrum and CF maxima that are narrower than that seen for Phobos and occur at lower frequencies (~1,000 cm^{-1}) than the average Phobos TES spectrum (1,133 cm^{-1}). In the absence of mid-IR spectroscopic evidence for an association between Phobos and a carbonaceous chondrite composition, we have compared the Phobos TES spectrum to other silicates that may provide evidence for Phobos' origin.

The mid-IR spectral properties of Tagish Lake and other carbonaceous chondrites (e.g., Donaldson Hanna et al., 2017) pose problems for the widely proposed asteroid capture hypothesis (Murchie et al., 1999, 2015; Pajola et al., 2012, 2013; Pang et al., 1978; Pollack et al., 1978; Rivkin et al., 2002) in addition to the dynamical issues related to the required high tidal dissipation rates required to explain Phobos' current orbit (Burns, 1992; Murchie et al., 2015; Rosenblatt, 2011). More recently, a Mars impact origin for Phobos has been suggested by several authors (Canup & Salmon, 2018; Craddock, 2011; Rosenblatt & Charnoz, 2012). This type of origin model is difficult to reconcile with a chondritic composition for Phobos, as would be suggested by an asteroid capture model described above.

Fraeman et al. (2014) analyzed CRISM data of Phobos and found weak 0.65 and 2.8-μm features associated with the red spectral unit. They hypothesized that these features could be caused by either (1) the presence of a highly desiccated Fe-bearing phyllosilicate or (2) Rayleigh scattering and absorption by nanophase metallic Fe and surficial O-H bonds caused by space weathering. To test the first hypothesis, we compare the spectrum of Phobos to thermally altered nontronite acquired under SPE conditions. In addition, we test a potential Mars crustal composition by comparing the Phobos spectrum to <10-μm Columbia River flood basalt (Thomson et al., 2014). Both samples were darkened by mixing 5 wt.% carbon black to approximate the visible albedo of Phobos.

The average TES spectrum of Phobos is shown with the basalt and thermally altered nontronite spectra in Figure 15. The thermally altered nontronite spectrum is a poor match to the main features seen in the Phobos spectrum. In addition, the CF position of the thermally altered nontronite spectrum occurs at much higher frequencies than is present in the Phobos spectrum, and it exhibits a sharp dropoff in emissivity toward higher frequencies. By contrast, the Phobos spectrum displays a broad CF emissivity maximum centered about 100 cm^{-1} higher than the altered nontronite CF. It is possible, however, that the sharp band seen at ~1016 cm^{-1} in the Phobos spectrum could be consistent with another phyllosilicate, as suggested by Giuranna et al. (2011).

The darkened thermally altered nontronite spectrum still displays a weak hydration feature near 1,600 cm^{-1}. While the average TES Phobos spectrum has a very weak feature in this region, it is more pronounced in the average spectrum of the red unit (Figure 8). This is consistent with the observation of a weak 2.8-μm feature seen in VNIR spectra of the red unit (Fraeman et al., 2014). The origin of this feature may be due to the presence of weakly hydrated minerals in the red unit regolith or through the interaction of the solar wind with Phobos' surface. The absence of a 2.8-μm or ~1,600-cm^{-1} feature in the blue unit could be due to dehydration/dehydroxylation of hydrated minerals as a result of the Stickney impact event or because of reduced space weathering of the blue unit. The latter scenario would seem to indicate a relatively young age for the Stickney impact event.

The major feature at ~825 cm^{-1} in the Phobos spectrum is relatively well matched by the transparency feature in the finely particulate basalt spectrum. The exact positions and shape of the features vary, but minor changes in chemistry (Ca/Na ratio in plagioclase) or mineralogy (plagioclase/pyroxene ratio) can cause

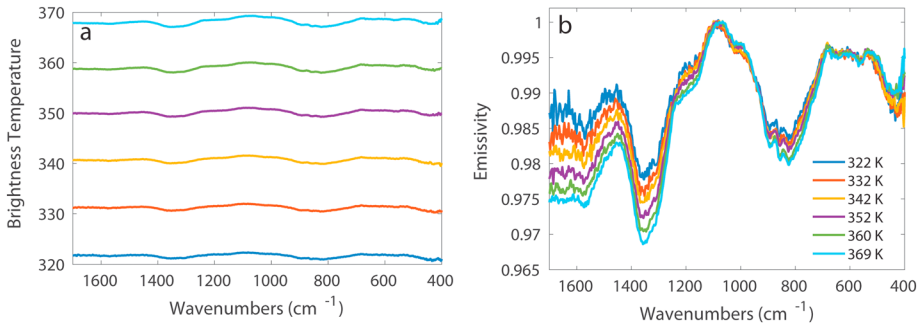

Figure 14. Spectra of Tagish Lake fines at different temperatures. (a) Brightness temperature spectra show the range of environmental conditions over which spectra were acquired. (b) Derived emissivity of Tagish Lake fines spectra. Despite temperatures that range over ~50 K, the spectra are nearly identical.

shifts in the position of this feature. In addition, the finely particulate basalt displays a broad rounded CF, centered only ~30 cm^{-1} shortward of the Phobos CF position. The basalt spectrum, however, does not display the strong minima at either 1,016 or 466 cm^{-1} that are seen in the Phobos spectrum.

If basalt is, indeed, a major component of the Phobos regolith, the general lack of mafic features in VNIR spectra (Fraeman et al., 2012, 2014; Murchie & Erard, 1996; Pieters et al., 2014; Rivkin et al., 2002) must be explained. Mature lunar regolith generally has a visible albedo ranging between ~0.05 and 0.1 (Ohtake et al., 2013), while the Phobos red and blue units have average visible albedos of ~0.05–0.06 and 0.08, respectively (Murchie & Erard, 1996). These albedos are similar, but fresh craters on lunar mare have typical albedos that are a few percent higher. However, Fraeman et al. (2012) showed that spectra of mature lunar soils and an average Mercury surface spectrum are still brighter than Phobos when corrected to the same viewing geometry, and exhibit weak mafic features, unlike the Phobos spectra. Still, the lower albedo of Phobos regolith compared to fresh mare craters could make mafic features more difficult to discern in VNIR spectra of Phobos, as demonstrated by the VNIR spectra of finely particulate basalt darkened by the addition of carbon lamp black (Figure 12).

The source of Phobos' low albedo, then, remains an important question. If Phobos is inherently dark because it is primarily composed of a carbonaceous material, then we would expect MIR spectra of those materials to match those of Phobos. Based on the (admittedly limited) work presented here and by Donaldson Hanna et al. (2017), this does not appear to be the case, although a more thorough analysis of relevant materials is certainly warranted in future work. It is well known that space weathering causes both darkening and reddening (Pieters & Noble, 2016) or, in some cases, just darkening (Lucey & Riner, 2011) of airless body surfaces. The degree of weathering is primarily dependent on the degree solar wind and micrometeoroid bombardment. The space weathering environment of Phobos and Deimos may be particularly intense, with heavy ion sputtering (sourced from Mars) perhaps exceeding that due to solar wind (Poppe & Curry, 2014). Additionally, Reddy et al. (2014) demonstrated that impact melt in the LL chondrite Chelyabinsk has a much lower overall albedo and greatly reduced mafic band depths than the mafic components. This process could not explain the dark, featureless VNIR spectrum of Phobos on its own as shock melt still retains some mafic features, but the presence of shock melt, in addition to the occurrence of intense space weathering, may further act to remove mafic spectral features in VNIR spectra.

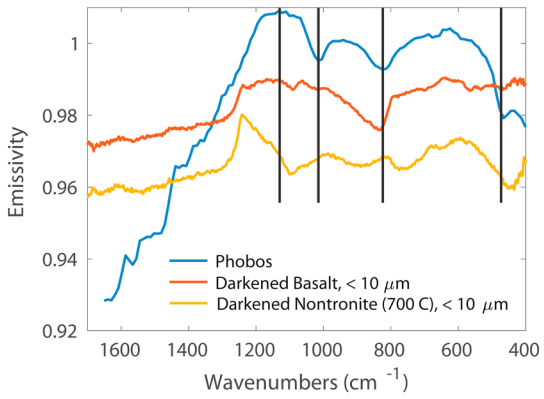

Figure 15. TES spectrum of Phobos with laboratory SPE spectra of basalt and thermally altered nontronite, both of which were darkened with carbon black to approximate the visible albedo of Phobos.

An additional factor to consider is average particle size of the Phobos surface. The thermal inertia of Phobos has been estimated to be ~25–80 $J \cdot m^2 \cdot K \cdot s^{1/2}$ (Lunine et al., 1982; Smith et al., 2018). These values correspond to effective particle sizes of at most a few tens of microns (Weschler et al., 1972). On the other hand, the average particle size of lunar regolith is ~60–80 μm, although the mean grain sizes of regolith samples returned by the Apollo astronauts range from 40 to 800 μm (McKay et al.,

1991). Very fine particulates, while brighter than coarser particulates of the same material, also exhibit weaker absorption features (e.g., Clark et al., 2003). The combination of lower albedo and finer particle size associated with the Phobos regolith could act to reduce or eliminate mafic absorption features that are common in mafic lunar soils.

If Phobos is composed partially or mostly of basalt, it must have a high porosity to account for its measured bulk density of 1,860 ± 13 kg/m^3 (Willner et al., 2014). Rosenblatt (2011) calculated required densities for Phobos and Deimos assuming a variety of compositions. Using lower and upper bounds of 2,500 and 3,500 kg/m^3 for a silicate composition, Rosenblatt (2011) estimated a macroporosity of 25–45% for Phobos. A high internal porosity is consistent with the presence of Stickney crater (Andert et al., 2010), as a large impact on a small body like Phobos would likely destroy it in the absence of that porosity (Richardson et al., 2002). In contrast, the bulk density of Tagish Lake (1,670 kg/m^3; Hildebrand et al., 2006) is lower than that of Phobos, and Rosenblatt (2011) argues that it would be difficult to compress such a material to the appropriate density for an object of Phobos' size.

A basaltic regolith on Phobos must also include another component to account for the 1,016 and 466-cm^{-1} features that are seen in the Phobos spectrum. Phyllosilicates and their thermal alteration and impact products display a variety of features near these positions (Che et al., 2011; Che & Glotch, 2012; Friedlander et al., 2015, 2016; Glotch et al., 2007), so a phyllosilicate or phyllosilicate-derived phase that we did not measure here could potentially account for those features. At lower frequencies (longer wavelengths), Fe oxides and oxyhydroxides commonly have spectral absorptions (Glotch et al., 2004; Glotch & Kraft, 2008; Glotch & Rossman, 2009), although none display a single, sharp peak at or near 466 cm^{-1}, as seen in the Phobos spectrum.

Sulfides are another intriguing possibility that could account for these spectral features. These minerals, which are common in chondritic meteorites, tend to be featureless throughout most of the mid-IR, with one or more strong features at $<$500 cm^{-1} (Brusentsova et al., 2012). Again, however, none of the phases that have been previously measured display a single sharp peak near ~466 cm^{-1}, as is seen for Phobos. Given the large variety of phyllosilicate chemistry and spectral properties, we suggest that it is most likely that a phyllosilicate phase, perhaps thermally desiccated, or impact-shocked, accounts for the spectral features of Phobos not well matched by finely particulate basalt. A minor portion of phyllosilicate-rich material derived from a chondritic impactor, mixed with a major component of Martian crustal material, would be consistent with this scenario.

5. Conclusions

We have remapped the detector footprints of Thermal Emission Spectrometer data onto Phobos using a new geometric processing routine and reassessed the composition of Phobos based on the presence of distinctive mid-IR spectral features. Previous VNIR spectroscopic studies of Phobos have likened it to D-class asteroids and the Tagish Lake meteorite based on the presence of a low albedo, featureless red slope at those wavelengths. We have demonstrated that the ungrouped C2 carbonaceous chondrite, Tagish Lake, is a poor mid-IR spectral match to the average TES spectrum of Phobos. We acquired spectra of finely particulate nontronite, thermally altered nontronite, and basalt, darkened with carbon black, under simulated Phobos environment conditions. Both nontronite and thermally altered nontronite are poor matches to the TES spectrum of Phobos, while the basalt spectrum matches some, but not all, features of the TES spectrum. It is possible that other phyllosilicates, or their desiccation or impact shock products, could be consistent with several features in the TES spectrum, although further detailed experimental work is required to support that suggestion.

Numerous objects exist in the solar system that are dark and/or featureless at VNIR wavelengths, making their compositions difficult or impossible to interpret based on VNIR reflectance spectra alone. The experience of TES at Phobos demonstrates that low-albedo airless bodies can display numerous interpretable features at mid-IR wavelengths and that these data should be utilized whenever possible, including upcoming missions to Bennu (Lauretta et al., 2017) and Jupiter Trojan asteroids (Levison & the Lucy Science team, 2016). Analysis of mid-IR data for airless bodies throughout the solar system must be supported by substantial laboratory work to characterize the appropriate analog materials under the appropriate environmental conditions.

Acknowledgments
This work was supported by the RIS^{4}E node (T. D. Glotch, PI) of NASA's Solar System Exploration Research Virtual Institute. TES footprint polygons and spectra and all laboratory spectra discussed in the text will be permanently archived at the Stony Brook University Academic Commons archive (https://commons.library.stonybrook.edu/). The authors gratefully acknowledge the detailed and constructive reviews of Drs. Matthew Izawa and Abigail Fraeman, whose reviews improved the content and clarity of the manuscript. The authors also thank Paul Lucey (U. Hawaii) for helpful discussions about the visible albedo of the lunar maria and Joel Hurowitz for providing the Columbia River basalt sample.

References

Andert, T. P., Rosenblatt, P., Pätzold, M., Häusler, B., Dehant, V., Tyler, G. L., & Marty, J. C. (2010). Precise mass determination and the nature of Phobos. *Geophysical Research Letters*, *37*, L09202. https://doi.org/10.1029/2009GL041829

Blinova, A. I., Zega, T. J., Herd, C. D. K., & Stroud, R. M. (2014). Testing variations within the Tagish Lake meteorite—I: Mineralogy and petrology of pristine samples. *Meteoritics and Planetary Science*, *49*(4), 473–502. https://doi.org/10.1111/maps.12271

Brown, P. G., Hildebrand, A. R., Zolensky, M. E., Grady, M., Clayton, R. N., Mayeda, T. K., et al. (2000). The fall, recovery, orbit, and composition of the Tagish Lake meteorite: A new type of carbonaceous chondrite. *Science*, *290*(5490), 320–325. https://doi.org/10.1126/science.290.5490.320

Brusentsova, T., Peale, R. E., Maukonen, D., Figueiredo, P., Harlow, G. E., Ebel, D. S., et al. (2012). Laboratory far-infrared spectroscopy of terrestrial sulphides to support analysis of cosmic dust spectra. *Monthly Notices of the Royal Astronomical Society*, *420*(3), 2569–2579. https://doi.org/10.1111/j.1365-2966.2011.20228.x

Burns, J. A. (1992). Contradictory clues as to the origin of the Martian moons. In H. H. Kiefer, et al. (Eds.), *Mars* (pp. 1283–1302). Tucson, AZ: University of Arizona Press.

Canup, R. M., & Salmon, J. (2018). Origin of Phobos-Deimos by the impact of a Vesta-to-Ceres sized body with Mars, Lunar Planet. Sci. XLVIV, Abstract 2598.

Che, C., & Glotch, T. D. (2012). The effect of high temperatures on the mid-to-far-infrared emission and near-infrared reflectance spectra of phyllosilicates and natural zeolites: Implications for Martian exploration. *Icarus*, *218*(1), 585–601. https://doi.org/10.1016/j.icarus.2012.01.005

Che, C., Glotch, T. D., Bish, D. L., Michalski, J. R., & Xu, W. (2011). Spectroscopic study of the dehydration and/or dehydroxylation of phyllosilicate and zeolite minerals. *Journal of Geophysical Research*, *116*, E05007. https://doi.org/10.1029/2010JE003740

Christensen, P. R., Bandfield, J. L., Hamilton, V. E., Ruff, S. W., Kieffer, H. H., Titus, T. N., et al. (2001). Mars Global Surveyor Thermal Emission Spectrometer experiment: Investigation description and surface science results. *Journal of Geophysical Research*, *106*(E10), 23,823–23,871. https://doi.org/10.1029/2000JE001370

Clark, R. N., Swayze, G. A., Livio, K. E., Kokaly, R. F., Sutley, S. J., Dalton, J. B., et al. (2003). Imaging spectroscopy: Earth and planetary remote sensing with the USGS Tetracorder and expert systems. *Journal of Geophysical Research*, *108*(E12), 5131. https://doi.org/10.1029/2002JE001847

Conel, J. E. (1969). Infrared emissivities of silicates: Experimental results and a cloudy atmospheric model of spectral emission from condensed particulate mediums. *Journal of Geophysical Research*, *74*(6), 1614–1634. https://doi.org/10.1029/JB074i006p01614

Cooper, B. L., Salisbury, J. W., Killen, R. M., & Potter, A. E. (2002). Midinfrared spectral features of rocks and their powders. *Journal of Geophysical Research*, *107*(E4), 5017. https://doi.org/10.1029/2000JE001462

Craddock, R. A. (2011). Are Phobos and Deimos the result of a giant impact? *Icarus*, *211*(2), 1150–1161. https://doi.org/10.1016/j.icarus.2010.10.023

Day, P. R. (1965). Particle fractionation and particle-size analysis. In C. A. Black, et al. (Eds.), *Methods of soil analysis. Part 1: Physical and mineralogical properties, including statistics of measurement and sampling* (pp. 545–567). Madison, WI: Am. Soc. Agron.

Donaldson Hanna, K. L., Schrader, D. L., Bowles, N. E., Clark, B. E., Cloutis, E. A., Connolly, H. C. Jr., et al. (2017). Spectral characterization of analog samples in anticipation of OSIRIS-REX's arrival at Bennu, Lunar Planet. Sci. XLVIII, Abstract 1723.

Emery, J. P., Cruikshank, D. P., & Van Cleve, J. (2006). Thermal emission spectroscopy (5.2-38 μm) of three Trojan asteroids with the Spitzer Space Telescope: Detection of fine-grained silicates. *Icarus*, *182*(2), 496–512. https://doi.org/10.1016/j.icarus.2006.01.011

Fraeman, A. A., Arvidson, R. E., Murchie, S. L., Rivkin, A., Bibring, J.-P., Choo, T. H., et al. (2012). Analysis of disk-resolved OMEGA and CRISM spectral observations of Phobos and Deimos. *Journal of Geophysical Research*, *117*, E00J15. https://doi.org/10.1029/2012JE004137

Fraeman, A. A., Murchie, S. L., Arvidson, R. E., Clark, R. N., Morris, R. V., Rivkin, A. S., & Vilas, F. (2014). Spectral absorptions on Phobos and Deimos in the visible/near infrared wavelengths and their compositional constraints. *Icarus*, *299*, 196–205.

Friedlander, L., Glotch, T. D., Phillips, B., Vaughn, J., & Michalski, J. R. (2016). Examining structural and related spectral change in Mars-relevant phyllosilicates after experimental impacts between 10-40 GPa. *Clays and Clay Minerals*, *64*(3), 189–209. https://doi.org/10.1346/CCMN.2016.0640302

Friedlander, L. R., Glotch, T. D., Bish, D. L., Dyar, M. D., Sharp, T. G., Sklute, E. C., & Michalski, J. R. (2015). Structural and spectroscopic changes to natural nontronite induced by experimental impacts between 10 and 40 GPa. *Journal of Geophysical Research: Planets*, *120*, 888–912. https://doi.org/10.1002/2014JE004638

Gaskell, R. W. (2011). Gaskell Phobos Shape Model V1.0. VO1-SA-VISA/VISB-5-PHOBOSSHAPE-V1.0. NASA Planetary Data System.

Gee, G. W., & Bauder, J. W. (1986). Particle-size analysis. In A. Klute (Ed.), *Methods of soil analysis. Part 1: Physical and Mineralogical Methods*, *Agron. Monogr.* (2nd ed., Vol. 9, pp. 383–411). Madison, WI: Am. Soc. Agron.

Giuranna, M., Roush, T. L., Duxbury, T., Hogan, R. C., Carli, C., Geminale, A., & Formisano, V. (2011). Compositional interpretation of PFS/Mex and TES/MGS thermal infrared spectra of Phobos. *Planetary and Space Science*, *59*(13), 1308–1325. https://doi.org/10.1016/j.pss.2011.01.019

Glotch, T. D., Bandfield, J. L., Lucey, P. G., Hayne, P. O., Greenhagen, B. T., Ghent, R. R., et al. (2015). Formation of lunar swirls by magnetic field standoff of the solar wind. *Nature Communications*, *6*(1), 6189. https://doi.org/10.1038/ncomms7189

Glotch, T. D., & Kraft, M. D. (2008). Thermal transformations of akaganéite and lepidocrocite to hematite: Assessment of possible precursors to Martian crystalline hematite. *Physics and Chemistry of Minerals*, *35*(10), 569–581. https://doi.org/10.1007/s00269-008-0249-z

Glotch, T. D., Morris, R. V., Christensen, P. R., & Sharp, T. G. (2004). Effects of precursor mineralogy on the thermal infrared emission spectra of hematite: Application to Martian hematite mineralization. *Journal of Geophysical Research*, *109*, E07003. https://doi.org/10.1029/2003JE002224

Glotch, T. D., & Rossman, G. R. (2009). Mid-infrared spectra and optical constants of six iron oxide/oxyhydroxide phases. *Icarus*, *204*(2), 663–671. https://doi.org/10.1016/j.icarus.2009.07.024

Glotch, T. D., Rossman, G. R., & Aharonson, O. (2007). Mid-infrared (5-100 μm) reflectance spectra and optical constants of 10 phyllosilicate minerals. *Icarus*, *192*(2), 605–622. https://doi.org/10.1016/j.icarus.2007.07.002

Henderson, B. G., & Jakosky, B. M. (1994). Near-surface thermal gradients and their effects on mid-infrared emission spectra of planetary surfaces. *Journal of Geophysical Research*, *99*(E9), 19,063–19,073. https://doi.org/10.1029/94JE01861

Henderson, B. G., & Jakosky, B. M. (1997). Near-surface thermal gradients and mid-IR emission spectra: A new model including scattering and application to real data. *Journal of Geophysical Research*, *102*(E3), 6567–6580. https://doi.org/10.1029/96JE03781

Herd, C. D. K., Blinova, A., Simkus, D. N., Huang, Y. S., Tarozo, R., Alexander, C. M. O., et al. (2011). Origin and evolution of prebiotic organic matter as inferred from the Tagish Lake meteorite. *Science*, *332*, 1304–1307.

Herd, C. D. K., Hilts, R. W., Skelhorne, A. W., & Simkus, D. N. (2016). Cold curation of pristine astromaterials: Insights from the Tagish Lake meteorite. *Meteoritics and Planetary Science*, *51*(3), 499–519. https://doi.org/10.1111/maps.12603

Hildebrand, A. R., McCausland, P. J. A., Brown, P. G., Longstaffe, F. J., Russell, S. D., Tagliaferri, E., et al. (2006). The fall and recovery of the Tagish Lake meteorite. *Meteoritics & Planetary Science*, *41*, 407–431.

Hilts, R. W., Herd, C. D. K., Simkus, D. N., & Slater, G. F. (2014). Soluble organic compounds in the Tagish Lake meteorite. *Meteoritics and Planetary Science*, *49*(4), 526–549. https://doi.org/10.1111/maps.12272

Hiroi, T., Zolensky, M. E., & Pieters, C. M. (2001). The Tagish Lake meteorite: A possible sample from a D-type asteroid. *Science*, *293*(5538), 2234–2236. https://doi.org/10.1126/science.1063734

Hyodo, R., Genda, H., Charnoz, S., & Rosenblatt, P. (2017). On the impact origin of Phobos and Deimos: I. Thermodynamic and physical aspects. *The Astrophysical Journal*, *845*(2), 125. https://doi.org/10.3847/1538-4357/aa81c4

Izawa, M. R. M., Flemming, R. L., King, P. L., Peterson, R. C., & McCausland, P. J. A. (2010). Mineralogical and spectroscopic investigation of the Tagish Lake carbonaceous chondrite by X-ray diffraction and infrared reflectance spectroscopy. *Meteoritics and Planetary Science*, *45*(4), 675–698. https://doi.org/10.1111/j.1945-5100.2010.01043.x

Lauretta, D. S., Balram-Knutson, S. S., Beshore, E., Boynton, W. V., Drouet D'Aubigny, C., DellaGiustina, D. N., et al. (2017). OSIRIS-REx: Sample return from asteroid (101955) Bennu. *Space Science Reviews*, 1–60. https://doi.org/10.1007/s11214-017-0405-1

Levison, H. F., & the Lucy Science team (2016). Lucy: Surveying the diversity of the Trojan asteroids: The fossils of planet formation, Lunar Planet. Sci. XLVII, Abstract 2061.

Logan, L. M., & Hunt, G. R. (1970). Emission spectra of particulate silicates under simulated lunar conditions. *Journal of Geophysical Research*, *75*(32), 6539–6548. https://doi.org/10.1029/JB075i032p06539

Logan, L. M., Hunt, G. R., Salisbury, J. W., & Balsamo, S. R. (1973). Compositional implications of Christiansen frequency maximums for infrared remote sensing applications. *Journal of Geophysical Research*, *78*(23), 4983–5003. https://doi.org/10.1029/JB078i023p04983

Lucey, P. G., Greenhagen, B. T., Song, E., Arnold, J. A., Lemelin, M., Donaldson Hanna, K., et al. (2017). Space weathering effects in Diviner Radiometer measurements of the lunar Christiansen Feature: Characteristics and mitigation. *Icarus*, *283*, 343–351. https://doi.org/10.1016/j.icarus.2016.05.010

Lucey, P. G., & Riner, M. A. (2011). The optical effects of small iron particles that darken but do not redden: Evidence of intense space weathering on Mercury. *Icarus*, *212*(2), 451–462. https://doi.org/10.1016/j.icarus.2011.01.022

Lunine, J. I., Negebauer, G., & Jakosky, B. (1982). Infrared observations of Phobos and Deimos from Viking. *Journal of Geophysical Research*, *87*(B12), 10,297–10,305. https://doi.org/10.1029/JB087iB12p10297

Lynch, D. K., Russell, R. W., Rudy, R. J., Mazuk, S., Venturini, C. C., Hammel, H. B., et al. (2007). Infrared spectra of Deimos (1-13 μm) and Phobos (3-13 μm). *Astronomy Journal*, *134*(4), 1459–1463. https://doi.org/10.1086/519975

Lyon, R. J. P. (1964). Evaluation of infrared spectrophotometry for compositional analysis of lunar and planetary soils: Part II. Rough and powdered surfaces. NASA Rep. CR-100 (264 pp.).

Matrajt, G., Borg, J., Raynal, P. I., Djouadi, Z., d'Hedencourt, L., Flynn, G., & Deboffle, D. (2004). FTIR and Raman analyses of the Tagish Lake meteorite: Relationship with the aliphatic hydrocarbons observed in the Diffuse Interstellar Medium. *Astronomy and Astrophysics*, *416*(3), 983–990. https://doi.org/10.1051/0004-6361:20034526

McKay, D. S., Heiken, G., Basu, A., Blanford, G., Simon, S., Reedy, R., et al. (1991). The Lunar Regolith. In G. H. Heiken, D. T. Vaniman, & B. M. French (Eds.), *Lunar sourcebook: A user's guide to the Moon* (Chap. 7, 305 pp.). Cambridge: Cambridge University Press.

Murchie, S., & Erard, S. (1996). Spectral properties and heterogeneity of Phobos from measurements by Phobos 2. *Icarus*, *123*(1), 63–86. https://doi.org/10.1006/icar.1996.0142

Murchie, S., Thomas, N., Britt, D., Herkenhoff, K., & Bell, J. F. III (1999). Mars Pathfinder spectral measurements of Phobos and Deimos: Comparison with previous data. *Journal of Geophysical Research*, *104*(E4), 9069–9079. https://doi.org/10.1029/98JE02248

Murchie, S. L., Thomas, P. C., Rivkin, A. S., & Chabot, N. L. (2015). Phobos and Deimos. In P. Michel, et al. (Eds.), *Asteroids IV* (pp. 451–467). Tucson, AZ: University of Arizona Press.

Ohtake, M., Pieters, C. M., Isaacson, P., Besse, S., Yokota, Y., Matsunaga, T., et al. (2013). One Moon, many measurements. 3: Spectral reflectance. *Icarus*, *226*(1), 364–374. https://doi.org/10.1016/j.icarus.2013.05.010

Osawa, T., Kagi, H., Nakamura, T., & Noguchi, T. (2005). Infrared spectroscopic taxonomy for carbonaceous chondrites from speciation of hydrous components. *Meteoritics and Planetary Science*, *40*(1), 71–86. https://doi.org/10.1111/j.1945-5100.2005.tb00365.x

Pajola, M., Lazzarin, M., Bertini, I., Marzari, F., Turrini, D., Magrin, S., et al. (2012). Spectrophotometric investigation of Phobos with the Rosetta OSIRIS-NAC camera and implications for its collisional capture. *Monthly Notices of the Royal Astronomical Society*, *427*(4), 3230–3243. https://doi.org/10.1111/j.1365-2966.2012.22026.x

Pajola, M., Lazzarin, M., Dalle Ore, C. M., Cruikshank, D. P., Roush, T. L., Magrin, S., et al. (2013). Phobos as a D-type captured asteroid, spectral modeling from 0.25 to 4.0 μm. *The Astrophysical Journal*, *777*(2), 127. https://doi.org/10.1088/0004-637X/777/2/127

Pang, K., Pollack, J., Veverka, J., Lane, A., & Ajello, J. (1978). The composition of Phobos: Evidence for carbonaceous chondrite surface from spectral analysis. *Science*, *199*(4324), 64–66. https://doi.org/10.1126/science.199.4324.64

Pieters, C. M., Murchie, S., Thomas, N., & Britt, D. (2014). Composition of surface materials on the Moons of Mars. *Planetary and Space Science*, *102*, 144–151. https://doi.org/10.1016/j.pss.2014.02.008

Pieters, C. M., & Noble, S. K. (2016). Space weathering on airless bodies. *Journal of Geophysical Research: Planets*, *121*, 1865–1884. https://doi.org/10.1002/2016JE005128

Pollack, J. B., Veverka, J., Pang, K. D., Colburn, D. S., Lane, A. L., & Ajello, J. M. (1978). Multicolor observations of Phobos with the Viking Lander cameras: Evidence for a carbonaceous chondritic composition. *Science*, *199*(4324), 66–69. https://doi.org/10.1126/science.199.4324.66

Poppe, A. R., & Curry, S. M. (2014). Martian planetary heavy ion sputtering of Phobos. *Geophysical Research Letters*, *41*, 6335–6341. https://doi.org/10.1002/2014GL061100

Presley, M. A., & Christensen, P. R. (1997). Thermal conductivity of particulate materials 2. *Results. Journal of Geophysical Research*, *102*, 6551–6566.

Reddy, V., Sanchez, J. A., Bottke, W. F., Cloutis, E. A., Izawa, M. R. M., O'Brien, D. P., et al. (2014). Chelyabinsk meteorite explains unusual spectral properties of Baptistina asteroid family. *Icarus*, *237*, 116–130. https://doi.org/10.1016/j.icarus.2014.04.027

Richardson, D. C., Leinhardt, Z. M., Melosh, H. J., Bottke, W. F. Jr., & Asphaug, E. (2002). Gravitational aggregates: Evidence and evolution. In B. Bottke, A. Cellino, P. Paolocchi, & R. Binzel (Eds.), *Asteroids III* (pp. 501–515). Tucson, AZ: University of Arizona Press.

Rivkin, A. S., Brown, R. H., Trilling, D. E., Bell, J. F. III, & Plassman, J. H. (2002). Near-infrared spectrophotometry of Phobos and Deimos. *Icarus*, *156*(1), 64–75. https://doi.org/10.1006/icar.2001.6767

Rogers, A. D., & Aharonson, O. (2008). Mineralogical composition of sands in Meridiani Planum from MER data and comparison to orbital measurements. *Journal of Geophysical Research*, *113*, E06S14. https://doi.org/10.1029/2007JE002995

Rosenblatt, P. (2011). The origin of the Martian moons revisited. *Astronomy and Astrophysics Review*, *19*, 19–44.
Rosenblatt, P., & Charnoz, S. (2012). On the formation of the Martian moons from a circum-Martian accretion disk. *Icarus*, *221*(2), 806–815. https://doi.org/10.1016/j.icarus.2012.09.009
Salemi, E., Tessari, U., Colombani, N., & Mastrocicco, M. (2010). Improved gravitational grain size separation method. *Applied Clay Science*, *48*(4), 612–614. https://doi.org/10.1016/j.clay.2010.03.014
Shirley, K. A., McDougall, D., & Glotch, T. D. (2018). The effect of albedo on mid-infrared spectra of airless bodies with implications for Diviner data analysis, Lunar Planet. Sci. XLVIV, Abstract 1298.
Simkus, D. N. (2017). The prebiotic synthesis of soluble organic matter in carbonaceous chondrites and the influence of asteroidal aqueous alteration, (PhD thesis). University of Alberta.
Smith, N. M., Edwards, C. S., Mommert, M., Trilling, D. E., & Glotch, T. D. (2018). Mapping the thermal inertia of Phobos using MGS-TES observations and thermophysical modeling, Lunar Planet. Sci. XLVIV, Abstract 2809.
Thomson, B. J., Hurowitz, J. A., Baker, L. L., Bridges, N. T., Lennon, A. M., Paulsen, G., & Zacny, K. (2014). The effects of weathering on the strength and chemistry of Columbia River Basalts and their implications for Mars Exploration Rover Rock Abrasion Tool (RAT) results. *Earth and Planetary Science Letters*, *400*, 130–144. https://doi.org/10.1016/j.epsl.2014.05.012
Wälisch, M. P., Willner, K., Oberst, J., Matz, K.-D., Scholten, F., Roatsch, T., et al. (2010). a new topographic image atlas of Phobos. *Earth and Planetary Science Letters*, *294*, 541–546.
Weschler, A. E., Glaser, P. E., & Fountain, J. A. (1972). Thermal properties of granulated materials. In J. W. Lucas (Ed.), *Thermal characteristics of the Moon* (pp. 215–241). Cambridge, MA: MIT Press.
Willner, K., Shi, X., & Oberst, J. (2014). Phobos' shape and topography models. *Planetary and Space Science*, *102*, 52–59.
Zolensky, M. E., Nakamura, K., Gounelle, M., Mikouchi, T., Kasama, T., Tachikawa, O., & Tonui, E. (2002). Mineralogy of Tagish Lake: An ungrouped type 2 carbonaceous chondrite. *Meteoritics and Planetary Science*, *37*(5), 737–761. https://doi.org/10.1111/j.1945-5100.2002.tb00852.x